Flowing atmospheric pressure afterglow for ambient ionization : reaction pathways revealed by modeling

Flowing atmospheric pressure afterglow for ambient ionization: Reaction pathways revealed by modeling

Maryam Aghaei and Annemie Bogaerts

Research group PLASMANT, Chemistry Department, University of Antwerp, Universiteitsplein 1, 2610 Antwerp, Belgium
maryam.aghaei@uantwerpen.be, annemie.bogaerts@uantwerpen.be

ABSTRACT: We describe the plasma chemistry in a helium flowing atmospheric pressure afterglow (FAPA) used for analytical spectrometry, by means of a quasi-1D plasma chemical kinetics model. We study the effect of typical impurities present in the feed gas, as well as the afterglow in ambient humid air. The model provides the species density profiles in the discharge and afterglow region and the chemical pathways. We demonstrate that H, N, and O atoms are formed in the discharge region, while the dominant reactive neutral species in the afterglow are O_3 and NO. He^* and He_2^* are responsible for Penning ionization of O_2, N_2, H_2O, H_2, and N, and especially O and H atoms. Besides, He_2^+ also contributes to ionization of N_2, O_2, H_2O and O through charge transfer reactions. From the pool of ions created in the discharge, NO^+ and $(H_2O)_3H^+$ are the dominant ions in the afterglow. Moreover, negatively charged clusters, like $NO_3H_2O^-$ and $NO_2H_2O^-$, are formed and their pathway is discussed as well. Our model predictions are in line with earlier observations in literature about the important reagent ions, and provide a comprehensive overview of the underlying pathways. The model explains in detail why helium provides a high analytical sensitivity, because of high reagent ion formation by both Penning ionization and charge transfer. Such insights are very valuable for improving the analytical performance of this (and other) ambient desorption/ionization source(s).

INTRODUCTION

Ambient desorption/ionization mass spectrometry (ADI-MS) has become very popular in analytical chemistry. It allows analyzing samples with little or no pretreatment in the open, ambient environment.[1-3] It is of interest across broad application areas, including pharmaceutical analysis, process chemistry, biological imaging, *in vivo* analysis, proteomics, metabolomics, forensics, and explosives detection.[3,4] Various types of ion sources have been applied, such as atmospheric pressure glow discharges (APGDs), corona and dielectric barrier discharges (DBDs), and microwave-sustained plasma sources[3-16]. When operated in helium, they produce energetic species that react with constituents of the ambient atmosphere to generate a host of reagent ions, including protonated water molecules and clusters, as well as other positive ions, such as NO^+ and O_2^+. The first group of these reagents can ionize target molecules by proton transfer (PT), while the latter group causes ionization by charge transfer (CT). Together, they can ionize both polar and non-polar species for analysis by MS. Moreover, such ionization is typically soft, i.e., little molecular fragmentation occurs.[17,18] In most ion sources, when the beam of excited and ionized helium and of the reagent ions is rather warm, or can be heated, and can thus directly desorb volatile species from a sample surface.[14,17,19] In case of DBD ion sources, when the afterglow has a temperature only slightly above room temperature, the flow of helium gas can cause the desorption of volatile species.[7,10]

Since the introduction of the first ambient MS source in 2004,[20] more than 30 different sources have emerged in this field.[3,18] However, in spite of the great interest, the chemical reaction pathways are barely understood, especially in plasma-based sources. The difficulty in understanding these sources is due to the complexity of the physical-chemical processes.

A very promising type of ambient ionization source is the APGD, which has been modified for use in the flowing afterglow mode as a chemical ionization source for organic mass spectrometry.[22-25] Commonly used APGDs do not have (or use) an afterglow region. This means that the analytes are directly introduced into the plasma and, so, they could create plasma instabilities.[3] In contrast, the so-called flowing atmospheric pressure afterglow (FAPA) has two separate regions: the plasma ignition zone (between two electrodes) and the afterglow, which is generated outside the chamber. The analytes are introduced into the latter region and therefore do not affect the inter-electrode plasma conditions.[26] The FAPA source was introduced by Andrade et al.[23] in 2008, and has been applied both for the ionization of compounds in the gas phase,[23,27] as well as for desorption – ionization for the direct analysis of solid compounds, such as metal complexes and drugs, as well as liquid compounds and recently liquid crystals employed in display devices.[5-7,19,25] Importantly, the FAPA source can be tuned in hardness, enabling it to produce either mainly molecular ion, fragment ion, or atomic ion mass spectra.[17,19,28-31]

Among the many plasma-based ambient MS sources, the FAPA source has certain advantages. It seems less affected by ionization matrix effects,[32] can produce higher gas temperatures and directly generate "negative reagent ions".[19,28,33] Its simple construction and DC power, as well as its high sensitivity and abundance of reagent ions, make the FAPA source a suitable candidate for exploring unique plasma processes and chemistries.[17,19,34,36] Furthermore, the FAPA source represents an easy to handle alternative ionization source to the traditional corona discharge used in ion mobility analyzers.[26,37]

To further enhance the application potential of the FAPA source in analytical chemistry, its behavior must be better understood. This can be achieved by experiments, as illustrated for example in.[17,19,26,28] Some FAPA source parameters were found to greatly influence reagent-ion production, such as the discharge current,[17,19,26] gas flow rate,[17,19,26] and the anode and MS front plate potential.[19] Also the effects of geo-

metrical parameters, such as the spatial location within the afterglow[17] and the distance between the electrodes,[26] have been studied. In addition, both the positive and negative ion mode were studied for a variety of analyte types.[28]

The main difficulty in optimization of the FAPA source is that the above parameters all depend on each other. This raises the need for more detailed investigation, e.g., by computer modeling, to reveal the dominant ionization mechanisms. Moreover, it may help to optimize the setup geometry, such as the so-called μ-FAPA.[38] By providing details on the gas flow patterns, computer modeling may for instance explain the effect of applying a discontinuous helium gas flow within the FAPA source for the analysis of gaseous samples,[39] leading to lower helium consumption.

Despite the popularity of ambient ionization sources in analytical chemistry, only a few computational studies have been performed to describe their behavior. Martens et al. have investigated the plasma processes in an APGD in He by means of 2D fluid and 3D Monte Carlo (MC) simulations, including 9 species (for a mixture of He and N_2) and 21 chemical reactions.[40] This study was focused on the discharge region and did not include the afterglow, characteristic for the FAPA. Ellis et al. presented a 2D fluid model for a helium DC glow discharge in a mixture of N_2 and H_2O used for ADI-MS.[41] Both the fluid dynamics of the flowing gases and the chemical kinetics were described, considering 16 species interacting in 40 reactions. The authors showed that changes in impurity levels of the He gas (due to N_2 and H_2O) had a large effect on the formation of water clusters. Moreover, changes in ambient humidity (varied from 3 to 90 %) affected the size of the $(H_2O)_nH^+$ ions, but not the overall number of ions. Note however that no He excimers were included in the model and the number of reactions to describe the ionization pathways was fairly limited, probably to limit the calculation time.

Recently, zero-dimensional (0D) chemical kinetics models are gaining increasing interest, as they can describe a detailed chemistry without too much computational effort. Such models have been applied to various other plasma applications (e.g.,[42-49]), but not yet in the context of ADI-MS sources, although the latter are characterized by a rich plasma chemistry. Therefore, we developed a 0D plasma chemistry model (or more precisely: quasi-1D model; see below) for a mixture of He, N_2, O_2 and H_2O, combined with a 2D fluid dynamics model for the FAPA source, including 91 species and 1437 reactions, for both discharge and afterglow region, in order to obtain deeper insight in the underlying chemical mechanisms. The model includes all possible reactions of He gas flowing into humid air, and provides for the first time detailed information on the most important reagents and their reaction pathways for both discharge and afterglow of the FAPA source.

MODEL DESCRIPTION

Figure 1a schematically illustrates the FAPA source, considered in the model. It consists of a cathode pin and anode disk, placed 7.5 mm apart in a cylindrically symmetric discharge cell. A glow discharge plasma is established by applying 450 V between both electrodes in atmospheric pressure helium. This yields ca. 11.25 W applied power, as reported in both experimental and computational studies for a typical FAPA source.[29,41] The helium gas can flow out of the discharge cell through an orifice with 1 mm diameter in the center of the disk electrode. Details of the geometry and operating conditions are summarized in Table S1 in the Supplementary Information (SI).

We performed 2D fluid dynamics simulations using COMSOL CFD Software, to calculate among others the gas velocity as a function of distance from the cathode (Figure 1b). The latter is used as input in the chemical kinetics model (see below). The gas flows through two orifices, i.e, the anode orifice (O_A), with the same pressure up- and downstream, and the MS sampler orifice (O_S), with a pressure difference between up- and downstream, i.e., 1 atm vs. 1 torr. This sudden pressure drop causes a sudden rise in velocity close to the sampler (Figure 1b). The velocities at O_A and O_S are calculated as 13.5 and 55 m/s, respectively, in agreement with measurements by Shelly et al. (private communication).

In order to describe the chemistry for a helium discharge with humid air components, we made use of a 0D (or quasi-1D) chemical reaction kinetics model. We considered a feed gas of He (99.999%), with 10 ppm impurities of a $N_2/O_2/H_2O$ mixture (7, 2 and 1 ppm, respectively), flowing into ambient air, with 50 % relative humidity.

We used the ZDPlasKin v. 2.0 code (Zero-Dimensional PLASma KINetics solver),[50] which we modified to be able to use experimental values in the model, such as gas temperature and applied voltage, as well as the calculated gas velocity profile. Thus, the model can be considered as semi-empirical. The model includes 91 different species (i.e., the electrons, various types of atoms and molecules in ground state and excited levels, radicals and ions (positive and negative); see Table S2 in SI), which react in 1437 reactions (i.e., 148 electron impact reactions, 71 electron-ion recombination reactions, 412 ion-ion, 399 ion-neutral and 407 neutral reactions), for both discharge and afterglow region. In short, elastic collisions between electrons and He atoms, electron impact ionization and excitation from the He ground state, the He^* metastable levels and the He excimer levels (He_2^*), as well as various ionization and dissociation reactions are considered. Electron impact collisions with the N_2, O_2, and H_2O molecules are also included, in both the discharge (where these species are present as impurity) and the afterglow region (when the plasma gas diffuses in open air). To build our chemistry set, we started from a plasma chemistry set developed in our group for an argon plasma jet expanding in humid air, for plasma medicine applications,[42] and expanded it based on two other chemistry sets, i.e., He-O_2 plasma in humid air[51] and He-H_2O plasma.[52] Furthermore, we updated the chemistry set to be more relevant for analytical chemistry purposes, i.e., by introducing more reagent ions, e.g., H_3O^+, NO^+, O_2^+, and $(H_2O)_nH^+$ (n = 1 to 7).[17] This extended reaction set makes it possible to predict both the dominant species densities and the concentrations of less abundant plasma species, which are identified as possibly important in analytical chemistry applications.[17]

For each species, we solve a continuity equation, based on production and loss rates, as defined by the chemical reactions. We solve these equations as a function of time for a small volume element, which moves along the symmetry axis, as defined by the gas velocity. Hence, although the continuity equations do not include transport terms (0D model), we can translate the calculated temporal variation into a spatial variation, i.e., as a function of distance from the cathode pin (hence quasi-1D model), by means of the gas velocity profile, obtained from the 2D fluid dynamics model (see Figure 1b). In addition, the gas temperature profile is adopted from experiments,[29] and defines the gas density profile, which deter-mines the chemical reaction rates. More information about the model is presented in SI (section S.b and S.c).

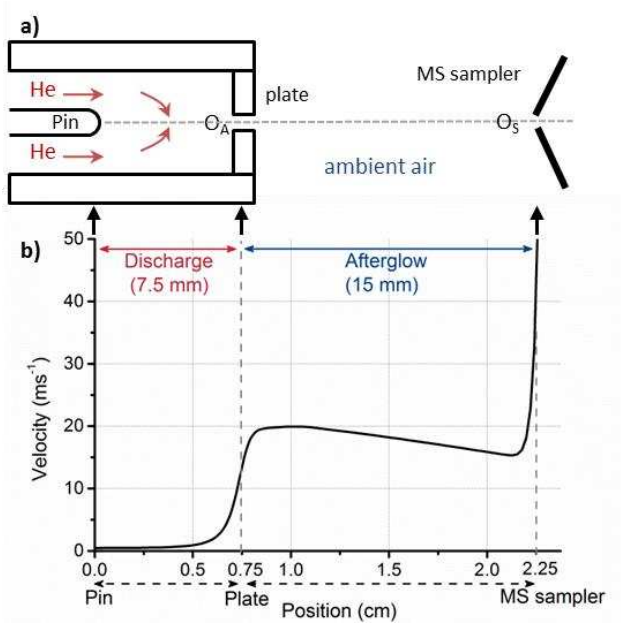

Figure 1. a) Scheme of the FAPA source: pin (cathode) and plate (anode), anode orifice (O_A), and sampler orifice (O_S). b) Calculated axial gas velocity profile through the discharge and afterglow, obtained by a 2D fluid dynamics model.

RESULTS AND DISCUSSION

(a) General plasma characteristics and species densities

Figure 2 presents the plasma characteristics along the symmetry axis of the FAPA source. The discharge ranges from the cathode (axial position 0 cm) till the anode (0.75 cm), while the afterglow ranges till the interface of the MS (2.25 cm). Note that the time and distance dimensions are correlated with a non-linear velocity profile (calculated with the fluid dynamics model; Figure 1b) due to the variable flow speed along the central axis.

Inside the discharge region, helium is the only dominant species, due to the low impurity levels, but in the afterglow, the densities of N_2, O_2 and H_2O gradually rise when the helium gas mixes with the humid air components. This is also observed in the air fraction, rising to 20% at the symmetry axis. The calculated electron temperature (T_e) is around 2.2 eV in the discharge region and roughly zero in the afterglow, because of absence of the electric field. The electron density is around 10^{13} cm^{-3} in the discharge region, and drops by four orders of magnitude in the first 1.5 mm of the afterglow, and to negligible values further in the afterglow, because of electron-ion recombination, as well as the absence of further electron impact ionization in the afterglow (cf. negligible T_e). This calculated electron density is in agreement with the measured electron density, i.e., 1.5 x 10^{19}m^{-3} for a FAPA source at 1.5 L/min helium flow rate.[29] Finally, the gas temperature is 750 K in the discharge region, and 500 K in the afterglow, as obtained from experiments[29] and used as input in the model. In Figure S1 in the SI, we compare the density profiles of various species in both discharge and afterglow region. Due to the different operating conditions in both regions, different chemistries take place. To better identify the importance of different species, we specify their densities at two points along the central axis in Table 1, i.e., near the end of the discharge (0.73 cm) and near the end of the afterglow (at 2 cm, i.e., 0.25 cm upstream the MS sampler). The species are listed in the order of decreasing density, separately for discharge and afterglow region, and for the afterglow region

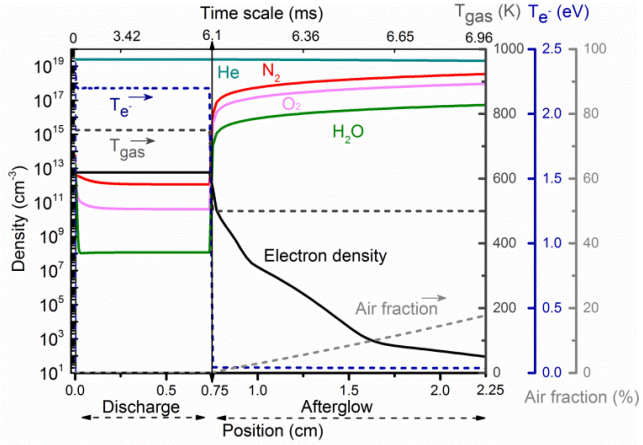

they are colored in green, black or red if their density increases, decreases or stays almost constant **Figure 2.** Plasma characteristics along the symmetry axis of the FAPA source. The gas temperature is used as input, while the electron temperature, species densities and air fraction are calculated in the model. The parameters in dashed lines are presented at the right axes.

compared to the discharge region. The excited species are not shown in this table, but they are listed in Table S4 in the SI. Here, we briefly discuss the species densities based on Table 1. A detailed discussion about the species densities, ionization degree and role of electrons is given in the SI (section S.e).

As far as the neutral species are concerned, it is shown in Table 1 that, apart from the initial compounds, i.e., He for the discharge and He, N_2, O_2 and H_2O for the afterglow, the N, O, H atoms are the dominant species (higher densities compared to the ions as well) in the discharge region, while O_3, NO, HO_2 and OH are most important in the afterglow. As shown in column 4 of Table 1 and Figure S1(c), NO^+ and several water clusters ($(H_2O)_nH^+$, with n=2-6) are predicted to be the dominant positive ions in the afterglow region, and they are responsible for the production of analyte ions (M^+) and protonated analyte ions (MH^+), respectively. The latter are reported to be the most commonly formed analyte ions in the FAPA source, indicating that the dominant reaction pathway is proton-transfer ionization.[17] Moreover, our model reveals that $NO_3H_2O^-$ and $NO_2H_2O^-$ are the main negative ions in the afterglow region (see bottom part of Table 1 and Figure S1(d)). Although most applications focus on the detection of positive ions, measurements in the negative mode are for most of the plasma-based ion sources also possible.[28,33,55] In this case, reagent ions can deprotonate the analyte molecules, creating $[M\text{-}H]^-$ quasimolecular ions, or the analyte molecules form adducts with NO_2^- and NO_3^- ions, yielding $[M\text{-}NO_2]^-$ and $[M\text{-}NO_3]^-$ ions, respectively.[28,33] Measurements in the negative ion mode are especially favorable when the analyte molecules exhibit a high gas-phase acidity, as is the case e.g. for carboxylic acids.[27,33] Note that at the beginning of the afterglow, the O_2^- density is higher than the other negative ion densities, but upon the presence of water molecules, it will convert to $O_2H_2O_2^-$ and further to NO_2^- (see section (c) below).

In the following sections, we will discuss in more detail the chemical pathways of helium species, and of the dominant neutrals and ions.

b) Role of helium species in producing reagent ions

In Figure 3, we plot the density profiles of the metastable He atoms (He^*), He excimers (He_2^*), and the helium ions (He^+ and He_2^+), and we also indicate the role of these He species in the chemical pathways inside the discharge region. For the sake of

Tabel 1. **Species number densities, in discharge and afterglow***

M^0 (cm^{-3})				M^+ (cm^{-3})			
Discharge		Afterglow		Discharge		Afterglow	
He	2.5×10^{19}	He	2.1×10^{19}	H^+	3.3×10^{12}	NO^+	3.7×10^{9}
N	2.6×10^{14}	N_2	2.9×10^{18}	O^+	1.6×10^{12}	$(H_2O)_3H^+$	9.5×10^{8}
O	1.0×10^{14}	O_2	7.7×10^{17}	O_2^+	5.5×10^{11}	$(H_2O)_2H^+$	1.2×10^{8}
H	4.6×10^{13}	H_2O	4.4×10^{16}	NO^+	2.3×10^{11}	$(H_2O)_4H^+$	1.1×10^{8}
NO	1.5×10^{12}	O_3	2.2×10^{14}	He_2^+	1.7×10^{11}	$(H_2O)_5H^+$	1.2×10^{6}
N_2	1.2×10^{12}	NO	8.8×10^{13}	N^+	1.8×10^{10}	$(H_2O)_6H^+$	1.4×10^{3}
NH	4.7×10^{11}	HO_2	1.0×10^{13}	N_2^+	1.1×10^{10}	NO_2^+	3.3×10^{2}
H_2	1.5×10^{11}	OH	9.1×10^{12}	HeH^+	5.9×10^{9}	H_3O^+	2.1x10
N_2O	7.9×10^{10}	NO_2	7.7×10^{12}	OH^+	1.4×10^{9}	$(H_2O)_7H^+$	1.4×10^{-1}
O_2	4.1×10^{10}	O	6.6×10^{12}	He^+	1.2×10^{9}	HeH^+	2.5×10^{-4}
NO_2	1.4×10^{10}	HNO_2	4.0×10^{12}	NO_2^+	1.4×10^{8}	H_3^+	2.2×10^{-5}
HNO	8.2×10^{9}	H_2O_2	2.2×10^{12}	N_4^+	1.9×10^{7}	$O_2H_2O^+$	2.4×10^{-9}
OH	2.1×10^{9}	H_2	1.0×10^{12}	H_2O^+	8.7×10^{6}	$(H_2O)_2^+$	1.7×10^{-9}
HNO_2	2.6×10^{8}	N	7.7×10^{11}	N_3^+	1.7×10^{6}	H_2O^+	3.2×10^{-10}
H_2O	1.1×10^{8}	N_2O	4.7×10^{11}	H_3^+	7.3×10^{5}	OH^+	3.0×10^{-10}
HO_2	8.5×10^{7}	HNO_3	4.2×10^{11}	H_2^+	3.7×10^{4}	O_2^+	2.0×10^{-10}
NO_3	5.0×10^{7}	NO_3	6.4×10^{10}	$O_2H_2O^+$	8.9×10^{3}	O_4^+	6.3×10^{-13}
HNO_3	4.5×10^{6}	N_2O_3	3.4×10^{9}	H_3O^+	3.4×10^{3}	N_4^+	6.2×10^{-13}
O_3	4.2×10^{6}	H	2.6×10^{9}	O_4^+	1.7×10^{2}	He^+	7.4×10^{-14}
N_2O_3	2.5×10^{5}	HNO	1.1×10^{7}	$(H_2O)_2H^+$	6.5×10^{-4}	H_2^+	7.3×10^{-14}
H_2O_2	8.2×10^{2}	NH	8.2×10^{6}	$(H_2O)_2^+$	2.0×10^{-4}	N^+	6.9×10^{-14}
HNO_4	1.6×10^{-2}	N_2O_5	3.6×10^{6}	$(H_2O)_3H^+$	1.6×10^{-14}	N_2^+	5.0×10^{-14}
N_2O_5	3.5×10^{-3}	N_2O_4	1.9x10^3	$(H_2O)_4H^+$	1.8×10^{-26}	O^+	3.1×10^{-15}
N_2O_4	8.4×10^{-5}	HNO_4	6.7×10^{-3}	$(H_2O)_5H^+$	3.3×10^{-40}	He_2^+	3.7×10^{-16}
				$(H_2O)_6H^+$	1.3×10^{-55}	N_3^+	2.0×10^{-20}
				$(H_2O)_7H^+$	2.2×10^{-72}	H^+	2.7×10^{-22}

M^- (cm^{-3})							
Discharge				Afterglow			
e^-	5.9×10^{12}	$NO_2H_2O^-$	4.3x10	$NO_3H_2O^-$	4.6×10^{9}	NO_3^-	2.0x10
O^-	4.7×10^{8}	NO_3^-	3.4	$NO_2H_2O^-$	2.5×10^{8}	O^-	2.7
NO_2^-	1.4×10^{6}	O_3^-	6.4×10^{-2}	NO_2^-	2.3×10^{4}	O_3^-	1.9×10^{-1}
O_2^-	2.3×10^{5}	$NO_3H_2O^-$	5.8×10^{-6}	$O_2H_2O^-$	1.3×10^{4}	NO^-	1.5×10^{-4}
H^-	1.5×10^{4}	$O_2H_2O^-$	5.8×10^{-10}	O_2^-	1.8×10^{2}	H^-	3.9×10^{-7}
NO^-	1.1×10^{3}	OH^-	6.5×10^{-15}	e^-	1.8×10^{2}	OH^-	4.2×10^{-15}

***The densities are listed in decreasing order, for the neutral species (M0), positive ions (M+), and negative ions and electrons (M-). Note that the order of importance in discharge region and afterglow is different. Species with lower, higher and similar densities in the afterglow with respect to the discharge region are indicated in red, green and black color, respectively. The densities of excited species are listed in SI (Table S4).**

clarity, in the text below we refer to the reaction numbers in Table S3 of the SI within brackets. Table S5 provides the reaction rates at two positions along the central axis, i.e., near the end of the discharge and near the end of the afterglow.

It is clear that both He_2^* and He^* are the dominant He species in the discharge region. Furthermore, the He_2^+ ions exhibit a higher density in the plasma than the He^+ ions, which is quite common in APGDs.[40,55] The higher He^* and He_2^* densities are due to the higher excitation rate than ionization rate of He, in spite of the lower cross sections, due to the lower threshold for excitation compared to ionization, i.e., 19.8 vs 24.6 eV.[56] More specifically, the He atoms are excited to He^* (1 in

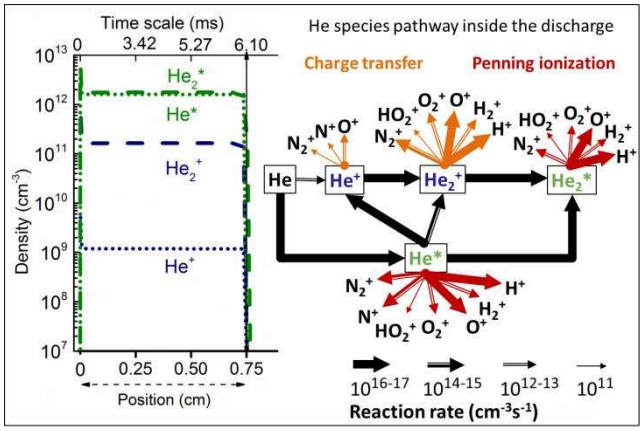

Figure 3 Number density profiles of the He species (left), and their reaction pathways in producing reagent ions (right), inside the discharge region. The thickness of the arrow lines indicates the magnitude of the corresponding reaction rate.

Table S3 of the SI) at a rate of 4.3×10^{17} $cm^{-3}s^{-1}$, and are then further converted to He_2^* (164) at a rate of 1.5×10^{17} $cm^{-3}s^{-1}$, while the ionization rate to He^+ (2) is only 7.7×10^{12} $cm^{-3}s^{-1}$, and the reaction to He_2^+ (93) occurs at a rate of 5.9×10^{16} $cm^{-3}s^{-1}$. Note that the main production of He^+ does not occur by ionization from the He ground state (2), but from He^* (3) with a reaction rate of 5.3×10^{16} $cm^{-3}s^{-1}$. He^* also contributes to the production of He_2^+ (166) at a rate of 8.1×10^{15} $cm^{-3}s^{-1}$. In Figure 3, the total formation rate of each species is illustrated by the thickness of each arrow line.

Figure 3 also depicts the role of the He species in producing reagent ions. In a helium discharge, commonly identified high-energy chemical species are He^*, He_2^*, He^+, and He_2^+.[29,58] Our model explains that the better analytical sensitivity with a He discharge compared with Ar and N_2 reported commonly in literature[10,17] is due to the high reagent ion formation rates, attributed to PI (red arrows) by He^* and He_2^* (i.e., 197, 213, 206, 207, 218, 206, 216, 227, and 208, in the order of decreasing reaction rate), and to some extent also to CT reactions (orange arrows) by He_2^+ and He^+ (i.e., 115, 130, 127, 128, 119, 94,131, 104, 105, 133, 98, and 108, in the order of decreasing reaction rate). As shown by the thickness of the arrow lines, He^* and He_2^+ are the dominant neutrals and ions, respectively, to ionize the molecules and atoms, by PI (arrows in red) and CT reactions (arrows in orange), respectively. This is in agreement with previous studies, in which He^* was considered the main species to produce reagent ions in helium-plasma ambient ionization sources.[12,29,57] It is generally agreed that He_2^+ is the dominant ion, with a higher density than He^+ ions in plasmas operated at pressures higher than 5 Torr.[58] Shelley et al. also observed He_2^* emission in a FAPA source,[29] which was not previously reported in spectroscopic studies of similar He APGDs. In previous modeling work for a helium APGD with limited chemistry set,[40] it was indicated that the number densities of He^* and He_2^* in the bulk of the plasma were approximately the same. Based on this, Shelley et al. suggested that it is reasonable to hypothesize that He_2^* serves as an energy carrier from the discharge to the atmosphere and would, thus, be an additional mechanism of reagent-ion formation. In our present study, we greatly extended the chemistry set, to include all major helium species and their full set of formation and loss reactions (i.e., 256 reactions with He species as reactant), and thus, Figure 3 gives a collective and complete over view of the He induced pathways, which covers and supports all separate former studies. Moreover, by means of this model we can illustrate in more detail the formation of

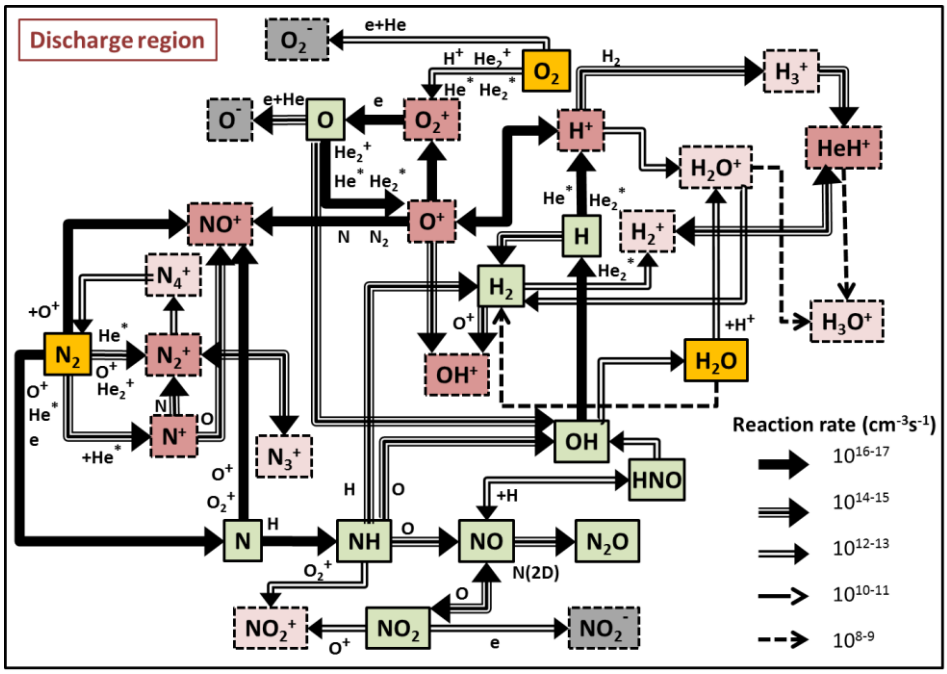

Figure 4 Reaction pathways of the most important species in the discharge region. The thickness of the arrow lines indicates the magnitude of the corresponding reaction rate. The air impurities are colored in yellow, the dominant formed neutrals in light green, the negative ions in gray and the positive ions in dark and light pink (for high or lower ion density, respectively).

specific reagent ions. For example, O^+, which plays an important role to produce NO^+, O_2^+, and OH^+ (see Figure 4), is formed in our model through 36 different reactions, and among them, 41% corresponds to three different He species: PI by He^* (26%, 197), CT from He_2^+ (9%, 117) and PI by He_2^* (6%, 213). On the other hand, for N^+, which is important to produce NO^+ and N_2^+, mainly He^* contributes to its formation (20%, 206), while He^+ has only a contribution of 0.07%. Likewise, H^+ is formed upon PI by He^* (contribution of 50%, 194), by He_2^* (contribution of 11%, 194), and by He_2^+ (contribution of 2%, 131), and it is important for the formation of H_2O^+, HeH^+ and OH^+, which are the main ions in the afterglow region to form water clusters. Although in all of the theoretical papers, He_2^+ is included in the chemistry set and also the experimental reports assumed it to be present, we did not find a direct measurement of He_2^+ in the literature. Therefore, we also performed simulations without formation of He_2^+, i.e., putting all He_2^+ formation rate coefficients equal to zero, as an extreme case, to test the effect on our calculations results. The results are presented in SI. We can conclude that removing He_2^+ affects the He^+ density (which becomes much higher), and that charge transfer ionization would not occur from He_2^+, but from He^+. However, all other results obtained from our model, including the other species densities and their formation pathways, would stay the same.

(c) Reaction pathways for the formation of reagent ions and reactive neutral species

Figure 4 and 5 present the reaction pathways for the dominant species in the discharge and afterglow region, respectively. The type of arrow lines represents the reaction rate (see legend) and different colors are used for neutrals and different ions. The humid air impurities, i.e., N_2, O_2, and H_2O, are shown in yellow. Since we discussed the He species pathways in previous section, here we only show these species close to each arrow as a reactant. The dominant positive ions (see Table 1, column 3) are shown in dark pink and those of lower importance are depicted in light pink. As the value of each arrow is specified in Figure 4 and 5, we do not repeat the reaction rates here in the text. Note that for each species there are several formation and loss reactions and we only mention the most important ones, for the sake of clarity, with the reaction numbers in parenthesis from Table S3.

N_2 forms several species via different type of reactions, including NO^+ (144), N_2^+ (959, 207, 127, 128, and 218), N^+ (206) and N atoms (144, 206, and 274). The first three are the dominant N-containing ions in the discharge region (see Table 1). N^+ reacts further with O (147 and 1071) into NO^+, and with N into N_2^+ (1070). The N atoms react with H into NH (240). Subsequently, in the presence of O and O_2^+, NH reacts further into NO (1419), N_2O (1256), NO_2 (253) and NO_2^+ (1041). Furthermore, NH also reacts into OH (1420), which is the primary source for the H atoms (308, 1427, 181, 311). The H atoms react further into H^+ upon PI by He^* (194) and He_2^*(211). The H^+ ions undergo CT with H_2O molecules, forming H_2O^+ (1060). Both H_2O and H_2O^+ are important species in the afterglow region to produce water clusters. In the discharge region, only H_3O^+ is formed (and no larger water clusters), either from HeH^+ (138) or H_2O^+ (1037). O_2 is ionized into O_2^+ upon reaction by H^+ (1058), He_2^+ (119), He^* (200) and He_2^* (216), and O_2^+ recombines with electrons into O atoms (405). The latter are ionized into O^+ by He^* (197), He_2^* (213), and He_2^+ (115). O^+ contributes to the formation of NO^+ upon reaction with N (1072) and N_2 (144). The CT reactions between H and O^+ (forming H^+ and O) and between O and H^+ (forming O^+ and H) occur with the same rate (1054 and 1057), so we used an arrow with two directions between O^+ and H^+ in Figure 4. There are other reactions with the same inverse reaction rate, which we did not plot in Figure 4, to keep the figure as clear as possible.

The main pathway for OH^+ formation is via O^+ and H_2 (1061) and the majority of H_2 is produced upon reaction of NH with

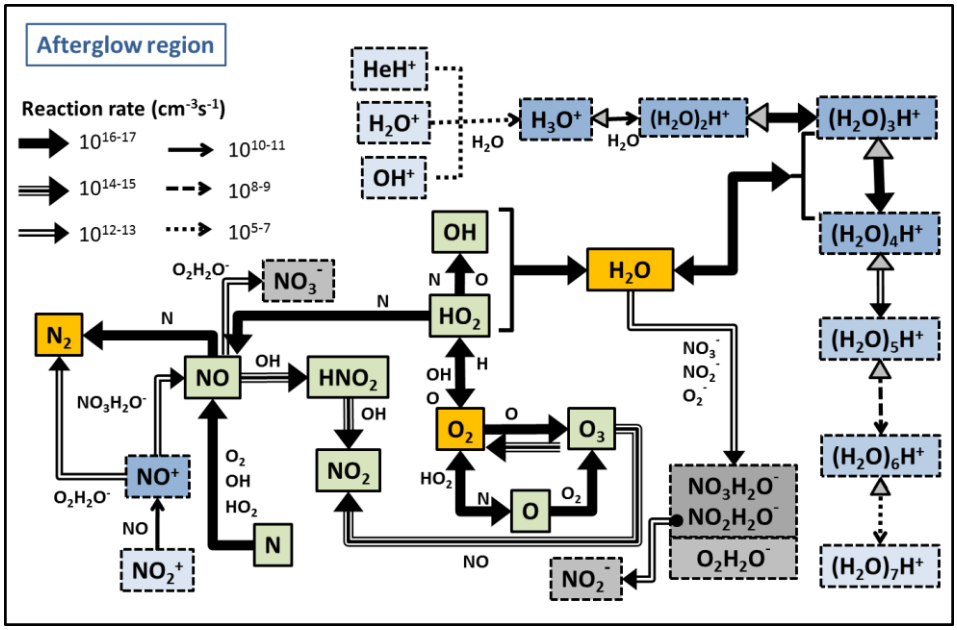

Figure 5 Reaction pathways of the most important species in the afterglow region. The thickness of the arrow lines indicates the magnitude of the corresponding reaction rate. The ambient (humid) air molecules are colored in yellow, the major neutrals are shown in light green, the negative ions in gray and the positive ions in dark and light blue (for high or lower ion density, respectively).

H atoms (1396).

As far as the dominant negative ions are concerned (see Table 1, and shown in Figure 4 in grey color), O^- and O_2^- are pro duced from O (7) and O_2 (8) by electron impact attachment in the presence of He, and NO_2^- is formed by electron impact attachment to NO_2 (273). As shown in Figure S1 and Table 1, the dominant species in the discharge are quite different from those in the afterglow region, and the pathways in the latter case are depicted in Figure 5. NO^+ is the dominant ion in the afterglow region. Beside the reactions shown in Figure 4, which are mainly responsible for making NO^+ a dominant ion, in the afterglow region NO_2^+ also converts to NO^+ (1043). This explains the drop in NO_2^+ density in the afterglow region. NO^+ partially recombines with negative ions and produces N_2 (572) and NO (498). The N atoms also produce more NO upon reaction with O_2 (1240), OH (1251) and HO_2 (1347), which explains the rise in NO density in the afterglow region. However, NO also reacts with N atoms to form back N_2 molecules (1243). In addition, both HNO_2 (233) and NO_2 (1342) are formed from NO upon reaction with OH.

O_2 forms O_3, either directly upon reaction with O atoms (250) or in a two-step process, by first dissociation to O upon react ion with N (240), and then recombining with O into O_3 (250). This explains the high density of O_3 in the afterglow. Note that O also recombines with HO_2 to form O2 again (1344). O_3 can also convert back to O_2 in several reactions (reactants not shown in Figure 5 for the sake of clarity), but its main loss pathway is the reaction with NO to produce O_2 and NO_2 (1235). However, the O3 formation rate is higher than the loss rate (cf. type of arrow lines in Figure 5).

Furthermore, O_2 also reacts with H atoms into HO_2 (231), which is one of the dominant neutrals in the afterglow, and it further reacts with N atoms into OH and NO (1347). HO_2 also reacts back into O_2 either by recombination with O (1344) or with OH (1340). The later also results in extra H_2O formation. H_2O partially reacts with negative ions (i.e., NO_3-, NO_2-, O_2-) into heavy negative ion clusters (85, 83, 918, respectively). Further on, $NO_2H_2O^-$ dissociates to H_2O and NO_2^-, either upon the presence of He (82) or O_2 (911). Note that in our model negative cluster ion formation is included, otherwise, NO_3^-, NO_2^- and O_2^- would be the dominant negative ions.

Our model shows that the main pathway of the water clusters in the afterglow region starts by the reaction of H_2O with HeH^+ (138), H_2O^+ (1081), and OH^+ (1068) to form H_3O^+, and subsequently the heavier ions. Indeed, the H_2O molecules in the presence of any other neutral (e.g., N_2, He, H_2, etc.) attach to a small cluster ion, to form the heavier ones. On the other hand, each of the water clusters, again in the presence of any neutral species, also dissociates back into H_2O and a smaller water cluster (1112-1123). That is why all the arrows between the water clusters have two directions, but with different colors (gray for the smaller rate and black for the slightly higher rate). We show both directions of these reactions in order to give a clear overview, especially for the water clusters, as they are important reagent ions for analytical purposes. In general, the formation of the heavier clusters from the smaller ones is a bit higher than in the opposite direction. In addition, the formation rate of the heavier clusters rises up to $(H_2O)_3H^+$ and then gradually decreases for increasing cluster size (see the thickness of the arrows in Figure 5), and this explains the order of the water cluster density in the afterglow region in Figure S1(c) and Table 1, i.e., $(H_2O)_3H^+$ has the highest density. In fact, in contrast to the other water clusters, $(H_2O)_3H^+$ has two main formation sources, since both $(H_2O)_2H^+$ and $(H_2O)_4H^+$ contribute with nearly the same reaction rate, one by consuming a water molecule (1114) and the other by releasing one (1117) (i.e., both arrows around $(H_2O)_3H^+$ have the same thickness in Figure 5). To summarize, the production of $(H_2O)_3H^+$ from $(H_2O)_2H^+$ (1114) and the production of $(H_2O)_4H^+$ from $(H_2O)_3H^+$ (1116) contribute together for 99% to the H_2O consumption in the afterglow region, while the inverse reactions (1115 and 1117) contribute for 69% to H_2O formation. The remaining H_2O formation mainly comes from the reaction of OH and HO_2 (29%, 1340) and the rest (2%) is from 272 other reactions.

As mentioned above, the protonated water clusters are very important reagent ions in analytical applications. The protonated water clusters protonate the sample molecules via

$(H_2O)nH^+ + M \rightarrow MH^+ + nH_2O$

For this ionization pathway to occur, the gas-phase acidity of the protonated water clusters and the gas-phase basicity of the analyte molecule are of crucial importance. However, since especially the smaller protonated water clusters (n = 1,2,3) exhibit very high gas-phase acidities, even compounds with a rather low gas-phase basicity are readily ionized by PT, yielding MH^+ quasimolecular ions.[8,28]

Besides the protonated water clusters, other positive reagent ions, such as NO^+ and NO_2^+, are also formed in the afterglow region, as also reported before.[17,19,28,33] These reagent ions can ionize sample compounds via charge-transfer processes, resulting in molecular ions, M^+, and thus, they offer alternative ionization routes besides PT, leading to a broader range of suitable analytes.

$NO^+ + M \rightarrow M^+ + NO$

Nevertheless, these ionization mechanisms may also lead to the formation of adducts and oxidation of the original analyte compounds, which limits the detection of the target analyte and therefore is less favorable for analytical purposes. However, Bruggemann et al. showed that oxidation processes occur only for low volatile compounds with long carbon chains and/or high molecular weights. Analytes with low molecular weights and relatively high vapor pressure compounds can easily be desorbed and transferred into the gas phase where subsequent ionization occurs.[28]

For either mechanism, i.e., proton or charge transfer, the greater the abundance of reagent ions available to transfer their charge to the analyte molecules, the higher the ionization probability and the less likely that competitive ionization will distort the observed spectra.[9] Badal et al.[17] found that the abundance and type of reagent ions produced by the FAPA source and the corresponding ionization pathways are different depending on the source operating conditions. A high abundance of proton-transfer reagent ions was observed with relatively high gas flow rates (1.5 L/min) and low discharge currents (5 mA). Vice versa, charge-transfer reagent species were most abundant at low gas flow rates (0.5 L/min) and high discharge currents (30 mA). Considering the extreme cases of 0.5 L/min and 30 mA, or 1.5 L/min and 5 mA, while the condition used in our study (1.5 L/min and 25 mA) is more intermediate and is reported as a typical operating condition of the FAPA source,[41] we may indeed expect to have both PT and CT reagent ions.

CONCLUSION

We developed a quasi-1D chemical kinetics model to study the chemical reaction pathways for reagent ion formation in a flowing atmospheric pressure afterglow (FAPA), used for ambient desorption/ionization mass spectrometry (ADI-MS). The model predicts the species density profiles in the discharge and afterglow region. We consider helium feed gas with 10 ppm impurity, which flows into the open atmosphere, assuming 50% relative humidity. For this purpose, we developed an extended reaction chemistry set for a helium/humid air mixture, which accounts for 91 different species and 1437 reactions.

Our calculations show that O, H and N atoms are formed with high densities inside the discharge region, in spite of the ppm impurities in the gas feed. In the afterglow, due to the absence of an electric field, as well as ambient air diffusion, and atom recombination, the densities of these atoms drop, while other species become more important, i.e., various N-O, H-O, N-H and N-H-O species. O_3 and NO are the dominant ones, and their densities increase strongly from the beginning of the afterglow region.

The electron density drops rapidly in the afterglow, due to dissociative attachment to positive ions (creating reactive neutral species) and to neutral species (creating negative ions). In addition, negatively charged heavy clusters, i.e., $NO_3H_2O^-$ and $NO_2H_2O^-$, are created in the afterglow through attachment of water molecules to NO_3^- and NO_2^- ions. Positive ions are mainly created through PI by He metastable species (He^* and He_2^*) and CT with He^+ and (especially) He_2^+ ions in the discharge region. O_2^+ and O^+ ions, which are important ions in the discharge, react with N and N_2 to form NO^+ ions, being the dominant ions in the afterglow. CT of N^+ with O atoms is also an important pathway for NO^+ formation. The most important positive ion in the discharge, i.e., H^+, forms HeH^+, H_2O^+ and OH^+ ions, which are in the afterglow quickly converted into H_3O^+ and protonated water clusters. The NO^+ ions and protonated water clusters are the two main type of reagent ions in analytical chemistry, important to ionize the analyte molecules by CT or PT into M^+ and MH^+, respectively.

Note that the formation of He_2^+ might be overestimated in our model, as we did not find a direct measurement of He_2^+ in literature. Therefore, to see the effect of He_2^+ in our model, we performed simulations without He_2^+. As illustrated by our results presented in the SI, our calculation results would change a bit. The main difference is that charge transfer ionization by He species would then not occur from He_2^+, but from He^+, which would have a much higher density, but all other results, including the other species densities and their formation pathways, would stay the same. In this study we focused on the plasma chemistry without any analyte, because not enough reliable reaction kinetics data is available in literature for a detailed description of the latter. Nevertheless, this model provides a comprehensive overview of the chemical pathways of a He-humid air plasma and afterglow, and forms the basis for any future studies on the addition of analytes, when data become available. Our model predictions are in line with earlier observations in literature about the important reagent ions. The model is applied here to the FAPA setup at a fixed condition, but it could also be applied to different geometries, different ambient humidity and different operational conditions, to study the most optimum conditions, as well as to other ADI-MS plasma sources operating at similar conditions.

Supporting Information

Geometrical and operating condition, Description of the 2D fluid dynamic model, Description of the 0D plasma chemical kinetics model, List of plasma species included in the model, List of reactions included in the model, Number densities of the most important species, Number densities of excited species, Discussion on role of electrons, List of reaction rates at the end of discharge and afterglow, Results and discussion for simulations without He_2^+

ACKNOWLEDGMENT

The authors gratefully acknowledge financial support from the Fonds voor Wetenschappelijk Onderzoek (FWO), grant number 6713. The computational work was carried out using the Turing HPC infrastructure at the CalcUA core facility of the Universiteit Antwerpen (UA), a division of the Flemish Supercomputer Center VSC, funded by the Hercules Foundation, the Flemish Government (department EWI) and the UA. The authors also thank J. T. Shelley for providing experimental data for the gas velocity behind the anode disc and before the mass spectrometer interface, to validate our model.

REFERENCES

(1) Van Berkel, G. J.; Pasilis, S. P.; Ovchinnikova, O. *J. Mass Spectrom*. **2008**, 43, 1161–1180.

(2) Cooks, R. G.; Ouyang, Z.; Takats, Z.; Wiseman, J. M. *Science*, **2006**, 311, 1566–1570.

(3) Shelley, J. T.; Badal, S. P.; Engelhard, C.; Hayen, H. *Anal. Bioanal. Chem.* **2018**, 410, 4061–4076.

(4) Weston, D. J. *Analyst*, **2010**, 135, 661–668.

(5) Kuhlmann, C.; Shelley, J. T; Engelhard, C. *J. Am. Soc. Mass Spectrom.* **2019** *30* (10), 2101-2113.

(6) Guć, M.; Schroeder, G. *Appl. Sci.* **2020**, *10*, 4217.

(7) Habib, A.; Ninomiy, S.; Chen, L. C.; Usmanov, D. T.; Hiraoka, K. J. *Am. Soc. Mass Spectrom*. **2014**, 25, 1177-1180.

(8) Cody, R. B.; Laramée, J. A.; Durst, H. D. *Anal. Chem.* **2005**, 77, 2297−2302.

(9) Shelley, J. T.; Wiley, J. S.; Chan, G. C.; Schilling, G. D.; Ray, S. J.; Hieftje, G. M. *J. Am. Soc. Mass Spectrom.* **2009**, 20, 837−844.

(10) Bi, L.; Habib, A.; Chen, L.; Xu, T.; Wen, L. *Talanta* **2021**, 222, 121673.

(11) Na, N.; Zhao, M.; Zhang, S.; Yang, C.; Zhang, X. *J. Am. Soc. Mass Spectrom.***2007,** 18, 1859-1862

(12) Klute, F. D.; Schutz, A.; Michels, A.; Vadla, C.; Veza, D.; Horvatic, V.; Franzke, J. *Analyst*, **2016**, 141, 5842–5848.

(13)Zhang, Y.; Ma, X. X.; Zhang, S. C.; Yang, C. D.; Ouyang, Z.; Zhang, X. R. *Analyst* **2009,** 134,176–181.

(14) Hendricks, P. I.; Dalgleish, J. K.; Shelley, J. T.; Kirleis, M. A.; McNicholas, M. T.; Li, L. F.; Chen, T. C.; Chen, C. H.; Duncan, J. S.; Boudreau, F.; Noll, R. J.; Denton, J. P.; Roach, T. A.; Ouyang, Z.; Cooks, R. G. *Anal. Chem*. **2014**, 86, 2900−2908.

(15) Wiley, J. S.; Shelley, J. T.; Cooks, R. G. *Anal. Chem*. **2013**, 85, 6545−6552.

(16) Zhan, X.; Zhao, Z.; Yuan, X.; Wang, Q.; Li, D.; Xie, H.; Li, X.; Zhou, M.; Duan, Y. *Anal. Chem.* **2013**, 85, 4512−4519.

(17) Badal, S. P.; Michalak, S.D.; Chan, G. C.-Y.; You, Y.; Shelley, J. T. *Anal. Chem*. **2016**, 88, 3494–3503.

(18) Cody, R. B. *Anal. Chem*. **2009**, 81, 1101−1107.

(19) Shelley, J. T.; Wiley, J. S.; Hieftje, G. M. *Anal. Chem*. **2011**, 83, 5741−5748.

(20) Takats, Z.; Wiseman, J. M.; Gologan, B.; Cooks, R. G. *Science* **2004**, 306, 471−473.

(21) Weston, D. J.; Ray, A. D.; Bristow, A. W. T. *Rapid Commun. Mass Spectrom*. **2011**, 25, 821–825.

(22) Shelley, J. T.; Hieftje, G. M. *J. Anal. At. Spectrom*. **2011**, 26, 2153−2159.

(23) Andrade, F. J.; Shelley, J. T.; Wetzel, W. C.; Webb, M. R.; Gamez, G.; Ray, S. J.; Hieftje, G. M. *Anal. Chem*. **2008**, 80, 2646−2653.

(24) Smoluch, M.; Mielczarek, P.; Silberring, *J. Mass Spectrom. Rev*. **2016**, 35, 22–34.

(25) Andrade, F. J.; Shelley, J. T.; Wetzel, W. C.; Webb, M. R.; Gamez, G.; Ray, S. J.; Hieftje, G. M. *Anal. Chem*. **2008**, 80, 2654−2663.

(26). Bouza, M.; Orejas, J.; López-Vidal, S.; Pisonero, J.; Bordel, N; Pereiro, R.; Sanz-Medel, A. Analyst, 2016, 141, 3437.

(27) Schilling, G. D.; Shelley, J. T.; Broekaert, J. A. C.; Sperline, R. P.; Denton, M. B.; Barinaga, C. J.; Koppenaal, D. W.; Hieftje, G. M. J. *Anal. At. Spectrom*. **2009**, 24, 34–40.

(28) Brüggemann, M.; Karu, E.; Hoffmann, T. *J. Mass Spectrom*. **2016**, 51 (2), 141–149.

(29) Shelley, J. T.; Chan, G. C.-Y.; Hieftje, G. M. *J. Am. Soc. Mass Spectrom*. **2012**, 23, 407−417.

(30) Dong, C.; Wang, W.; Li, H. *Anal. Chem*. **2008**, 80, 3925–3930.

(31) Schwartz, A. J.; Shelley, J. T.; Walton, C. L.; Williams, K. L.; Hieftje, G. M. *Chem. Sci.* **2016**, 7, 6440–6449.

(32) Shelley, J. T.; Hieftje, G. M.; *J. Anal. At. Spectrom.* **2010**, 25, 345–350.

(33) Gross, J. H. *Anal. Bioanal. Chem*. **2013**, 406 (1), 63–80.

(34) Jecklin, M. C.; Gamez, G.; Touboul, D.; Zenobi, R .*Rapid Commun. Mass Spectrom*. **2008**, 22, 2791–2798.

(35) Schaper, J. N.; Pfeuffer, K. P.; Shelley, J. T.; Bings, N. H.; Hieftje. G. M. *Anal. Chem*. **2012**, 84, 9246–9252.

(36) Brüggemann, M.; Karu, E.; Stelzer, T.; Hoffmann, T. *Environ. Sci. Technol*. **2015**, 49, 5571–5578.

(37) Golubovskii, Y. B.; Maiorov, V. A.; Behnke, J.; Behnke, J. F.; *J. Phys. D: Appl. Phys*. **2003**, 36, 39–49.

(38) Zeiri, O.M.; Storey, A.P; Ray, S.J.; Hieftje, G.M. *Anal. Chem. Acta*, **2017**, 952, 1–8 .

(39) Storey, A.P.; Zeiri, O.M.; Ray, S.J.; Hieftje, G. M. *J. Am. Soc. Mass Spectrom*. **2017**, 28, 263–269.

(40) Martens, T.; Mihailova, D.; van Dijk, J.; Bogaerts, A. *Anal. Chem*. **2009**, 81, 9096–9108.

(41) Ellis, W. C.; Spencer, R. L.; Reiningera, C.; Farnsworth, P. B. J. *Anal. At. Spectrom*. **2017**, 32, 2407–2415.

(42) Van Gaens, W.; Bogaerts, A. *J. Phys. D: Appl. Phys*. **2013**, 46, 275201 (53 pages).

(43) Heijkers, S.; Aghaei, M.; Bogaerts, A. J. *Phys. Chem. C.* **2020**,124 (13), 7016–7030, 2020

(44) Kogelschatz, U. *Plasma Chem. Plasma Process*. **2003**, 23, 1–46.

(45) Wagner, H.E.; Brandenburg, R.; Kozlov, K. V.; Sonnenfeld, A.; Michel, P.; Behnke, J. F. *Vacuum*, **2003**, 417–436.

(46) Slaets, J.; Aghaei, M.; Ceulemans, S.; Van Alphen, S.; Bogaerts, A. *Green Chem.* **2020**, 22 (4), 1366–1377.

(47) Vervloessem, E.; Aghaei, M.; Jardali, F.; Hafezkhiabani, N.; Bogaerts, A. *ACS Sustainable Chem. Eng*. **2020**, 8, 26, 9711–9720

(48) Aerts, R.; Tu, X.; Van Gaens, W.; Whitehead, J.C.; Bogaerts, A. *Environ. Sci. Technol*. **2013**, 47, 6478–6485.

(49) Wang, W.; Patil, B.; Heijkers, S.; Hessel, V.; Bogaerts, A. *ChemSusChem.* **2017**, 10, 2145–2157.

(50) Pancheshnyi, S.; Eismann, B.; Hagelaar, G.J.M.; Pitchford, L.C. Computer code ZDPlasKin, http://www.zdplaskin.laplace.univ-tlse.fr (University of Toulouse, LAPLACE, CNRS-UPS-INP, Toulouse, France, 2008).

(51) Murakami1, T.; Niemi, K.; Gans, T.; O'Connell, D.; Graham, W. G. *Plasma Sources Sci. Technol*. **2013**, 22 015003 (29pages)

(52) Liu, D. X.; Bruggeman, P.; Iza, F.; Rong, M. Z.; Kong, M. G. *Plasma Sources Sci. Technol*. **2010**, 19 025018 (22pages)

(53) Gielniak, B.; Fiedler, T.; Broekaert, J.A.C. *Spectrochim Acta Pt. B–Atom. Spectr*. **2011**, 66, 21–27.

(54) Ren, X.; Liu, J.; Zhang, C.; Luo, H.; *Rapid Commun. Mass Spectrom*. **2013**, 27 (5): 613–620.

(55) Shon, J. W.; Kushner, M. J. J. Appl. Phys. 1994, 75, 1883–1890.

(56) Bogaerts, A.; Gijbels, R. J. Appl. Phys. 2002, 92, 6408–6422.

(57) Ratcliffe, L.V.; Rutten, F.J.M.; Barrett, D.A.; Whitmore, T.; Seymour, D.; Greenwood, C.; Aranda-Gonzalvo, Y.; Robinson, S.; McCoustra, M. *Anal. Chem*. **2007**, 79, 6094–6101.

(58) Chan, G.C.Y.; Shelley, J.T.; Wiley, J.S.; Jackson, A.U.; Engelhard, C.; Cooks, R.G.; Hieftje, G.M. *Anal. Chem.* 2011, 83, 3675–3686.

Table of Contents artwork